# An MDO-based methodology for static aeroelastic scaling of wings under non-similar flow

Joan Mas Colomer, Nathalie Bartoli, Thierry Lefebvre, Joaquim R R A Martins, Joseph Morlier

**Structural and Multidisciplinary Optimization manuscript No.**
(will be inserted by the editor)

# An MDO-Based Methodology for Static Aeroelastic Scaling of Wings Under Non-Similar Flow

**Joan Mas Colomer · Nathalie Bartoli · Thierry Lefebvre · Joaquim R. R. A. Martins · Joseph Morlier**

Received: date / Accepted: date

**Abstract** The classical aeroelastic scaling theory used to design scaled models is based on the assumption that complete flow similarity exists between the full aircraft and the scaled model. When this condition is satisfied, the scaling problem of the model can be treated as a structural design problem only, where the scaled aerodynamic shape is preserved. If, on the other hand, this hypothesis no longer holds—if the scaled model is constrained to fly at low speed and low altitude, for example—and both the aerodynamic shape and the flexibility of the structure are exactly scaled, then the static response exhibits significant discrepancies in the aerodynamic loads and structural displacement. To design a flying demonstrator with scaled static response when flow similarity cannot be fulfilled, we present a multidisciplinary optimization based method that allows some freedom in the design of the wing shape (while keeping the scaled wingspan) to update the wing geometry and structural properties to ensure equivalent scaled loads and overall wing displacement. To illustrate this method, we apply it to a 1:5 version of the uCRM wing at subsonic flight condition. While the errors in air loads using the classical theory are around 16%, the presented method achieves errors lower than 1%, with a good agreement for the wingtip displacement.

**Keywords** Aeroelastic Scaling · Multidisciplinary Design Optimization · Aircraft Design

J. Mas Colomer
Institut Clément Ader, Université de Toulouse, ISAE-SUPAERO-CNRS-INSA-Mines Albi-UPS, Toulouse, France

N. Bartoli
ONERA/DTIS, Université de Toulouse, Toulouse, France
E-mail: nathalie.bartoli@onera.fr

T. Lefebvre
ONERA/DTIS, Université de Toulouse, Toulouse, France
E-mail: thierry.lefebvre@onera.fr

J. R. R. A. Martins
University of Michigan, Ann Arbor, United States of America
E-mail: jrram@umich.edu

J. Morlier
Institut Clément Ader, Université de Toulouse, ISAE-SUPAERO-CNRS-INSA-Mines Albi-UPS, Toulouse, France
E-mail: joseph.morlier@isae-supaero.fr

## Nomenclature

| | |
|---|---|
| $()^c$ | Relative to the cruise condition |
| $()^m$ | Relative to the scaled model |
| $()^r$ | Relative to the reference aircraft |
| $()^T$ | Transpose of a matrix or vector |
| $\beta$ | Radial basis function coefficient |
| $\delta\mathbf{u_a}$ | Virtual displacements on aerodynamic grid points |
| $\delta\mathbf{u_s}$ | Virtual displacements on structure nodes |
| $\delta W$ | Virtual work |
| $\gamma$ | linear polynomial coefficient |
| $\Lambda$ | Wing sweep angle |
| $\lambda_l$ | Global length ratio |
| $\lambda_\omega$ | Natural frequency ratio |
| $\lambda_\rho$ | Air density ratio |
| $\lambda_m$ | Total mass ratio |
| $[\mathbf{H}]$ | Displacement interpolation matrix |
| $\phi$ | Radial basis function |
| $\rho$ | Air density |
| $\sigma_y$ | Yield stress |
| $\sigma_{VM}$ | von Mises stress |
| $\theta_r$ | Wing mounting angle |
| $c$ | wing chord |
| $C_L$ | 3D Lift coefficient |
| $C_l$ | 2D lift coefficient |
| $E$ | Elastic modulus |

| | |
|---|---|
| $f$ | Objective function |
| $f_a$ | Aerodynamic forces on aerodynamic grid points |
| $f_s$ | Aerodynamic forces on the structural nodes |
| $h$ | Beam height |
| $I$ | Beam bending inertia |
| $k$ | Airfoil relative thickness scaling factor |
| $L$ | Beam length |
| $l$ | lift per unit span |
| $M$ | Mach number |
| $m$ | Total beam mass |
| $S$ | Wing surface |
| $s$ | Stringer cross section |
| $t$ | Plate thickness |
| $TPS$ | Thin plate spline |
| $u_a$ | Aerodynamic grid displacements |
| $u_s$ | Structural node displacements |
| $u_{tip}$ | Wingtip displacement |
| $V$ | Airspeed |
| $W$ | Aircraft weight (in mass units) |
| $w$ | Beam width |

## 1 Introduction

Searching for more efficient airplane designs drives aerospace engineers to investigate innovative solutions, such as the blended wing body, the box wing, or the strut-braced wing aircraft configurations. Whereas the conventional tube-and-wing configuration is well known and studied, the in-flight behavior of these new aircraft types often remains unknown. The development, construction, and experimentation of unmanned aeroelastically-scaled prototypes is a way to study the in-flight behavior of these innovative aircraft configurations. This mitigates the economical and operational risk of building and testing a full-scale prototype. In addition, aeroelastically-scaled prototypes can be used to show the impact of current aircraft layout modifications (e.g., an engine upgrade) on the in-flight response.

Traditional aeroelastic scaling theory of aircraft considers that the nondimensional fluid characteristics of the full-scale aircraft are preserved, or that the effect of their discrepancy (particularly the Mach number) can be neglected. However, attaining the same Mach number is sometimes impossible given the operational boundaries of the scaled unmanned prototypes.

Bisplinghoff et al. (1996) defined the basics of classical aeroelastic scaling theory in 1955. Scruton and Lambourne (1971) expanded the method to include the implications of thermal transfer and compressibility. To match the static characteristics of finite-element models intended for aeroelastic scaling, French (1990) presented an optimization-based strategy. French and Eastep (1996) later proposed a two-step strategy to also include dynamic aeroelastic scaling. First, they designed the structure by minimizing the discrepancies in static displacements. Then, they determined the values of non-structural masses through a minimization problem where the difference in mode shapes was minimized and the reduced modal frequencies were set as equality constraints.

Pereira et al. (2007) defined a method that optimized the natural frequencies and applied it to the design of a joined-wing wind tunnel scaled prototype to obtain equivalent dynamic and static aeroelastic scaling. Bond et al. (2012) proved that in addition to matching the natural frequencies, fitting the corresponding vibration modes is also required. Richards et al. (2009) established a comparison between a direct modal one-step strategy and a two-step methodology where the modal optimization was performed after establishing the stiffness distribution.

Like Bond et al. (2012), other authors have accounted for static scaling nonlinearities, extending the strategy outlined by French and Eastep (1996) to include geometric nonlinearities in the aeroelastic scaling method. Ricciardi et al. (2012) adapted the two-step strategy suggested by Richards et al. (2009) to include the equivalent nonlinear static deflections in the first optimization cycle. These two approaches were developed in the context of the experimental testing of a joined-wing SensorCraft prototype. Ricciardi et al. (2014) later proposed to use a single-step strategy where linear and nonlinear static responses were scaled while satisfying the natural frequency constraints. Wan and Cesnik (2014) provided a scaling method considering geometrical nonlinearities for very flexible airplanes, extending the linear scaling factors and similarity rules. Recently, Ricciardi et al. (2016) described a systematic strategy for the definition of scaled prototypes that are equivalent in terms of the aeroelastic properties. They proposed an optimization formulation that sought to match vibration and buckling modes, as well as the linear static displacements. They also highlighted the mode swapping and mixing phenomenon in the optimization process. Mas Colomer et al. (2017) discussed the issue of aeroelastic scaling when flow similarity is not matched exactly. They also discussed the issue of mode crossing through the implementation of a mode tracking approach in the framework of classic aeroelastic scaling (i.e., with presumed flow similarity). Cavallaro and Demasi (2016) offered a thorough literature study on the works related to the joined-wing SensorCraft prototypes for aeroelastic scaling. Additionally, Afonso et al. (2017) assessed the state-of the-art on the topic of nonlinear aeroelastic scaling of wings presenting a high aspect ratio. Spada et al. (2017) illustrated

the implementation of the two-step technique to high aspect ratio wings. More recently, Pontillo et al. (2018) introduced a suite of techniques for the design of a cantilevered wing model that replicates the static and dynamic response of a conceptual prototype. Regarding the dynamic aeroelasticity and multidisciplinary optimization, Jonsson et al. (2019) analyzed how flutter constraints can be integrated into multidisciplinary optimization of aircraft earlier in the design phase.

All the mentioned references assume that flow similarity is ensured between the two scales, or that at least the discrepancies in nondimensional airflow parameters (e.g., Mach and Reynolds numbers) can be neglected. This may not, however, be applicable to some flying prototypes with a limited flight envelope (in terms of altitude and speed). Consequently, it is necessary to establish a method for the design of aeroelastically scaled models that exhibit the same scaled aeroelastic behavior.

In general, classical aeroelastic scaling theory is based on the fact that flow similarity exists between the two scales. The existing works cited in this article assume flow similarity or expect that the existing differences are small enough to be neglected.

In this paper, we propose a methodology to establish the design of scaled aircraft wings in the case where the differences in the nondimensional airflow conditions result in substantial discrepancies in the static response (i.e., in the total aerodynamic load and structural wing deflection). To do so, we maximize the static aeroelastic similarity of the wing as a whole—in terms of the scaled total force and wing deflection. Once the airflow is not similar, the local data of the flow field and the structural response cannot be used to extrapolate the local response of the full-size aircraft.

To address this issue, we propose a multidisciplinary design optimization (MDO) approach to modify the geometry of the wing (while preserving the overall scaled span) and the structural properties simultaneously to obtain an equivalent scaled response (in terms of the total load and overall wing deflection).

Typically, MDO in the context of aircraft design is applied to maximize performance, such as aircraft mass or fuel burn. For example, Kenway and Martins (2014) apply high-fidelity aerostructural MDO to solve takeoff mass and fuel burn minimization problems. However, unlike typical applications, in this paper we use MDO to minimize the differences in the aeroelastic response between a scaled model and its full-size counterpart.

Given an MDO problem, there are many architectures that can be used to solve it. The work by Martins and Lambe (2013) presents a survey of all the available architectures for MDO problems. As we will detail on Section 2.3, in this paper we use the multidisciplinary feasible (MDF) approach.

The method that we propose is intended to be used to assess the static aeroelastic qualities of a given aircraft configuration, by matching the overall wing load and deflection, if flow similarity cannot be achieved.

## 2 Optimization Problem for Static Aeroelastic Similarity

In this paper, we focus on the static aeroelastic scaling in the case where flow similarity cannot be achieved. This is motivated by the limitations in altitude and speed of scaled flight demonstrators, which make it impossible to match both Mach number and Reynolds number. As shown by Bisplinghoff et al. (1996), preserving both shape and flow parameters is a requirement for complete aeroelastic similarity. Therefore, if there is no flow similarity, the final deformed state cannot be matched if the scaled structural stiffness and the aerodynamic shape are kept constant.

The goal of this paper is to develop a method for designing a scaled wing model whose overall deflection is as close as possible to the scaled response of the full-scale aircraft for the same angles of attack, even in the presence of a non-similar flow in the scaled model. To achieve this goal, we relax some geometrical design variables, namely the chords that define the wing planform, as well as the sweep angle and the mounting angle of the wing. The geometrical design variables have an impact on the stiffness of the wing because they determine the shape of the wingbox. Apart from these geometrical variables, we also set structure-specific variables for the wingbox properties (e.g., panel thicknesses and stringer sections).

### 2.1 Effect of Flow Similarity on Static Aeroelastic Scaling

In the case where there is flow similarity (shown in Figure 1), no aerodynamic analysis is required to ensure complete aeroelastic similarity between both scales because the load equivalence is guaranteed through a nondimensional analysis of the aerodynamic equations.

In practice, it might not be possible to match the Mach number due to the operational limitations in airspeed and altitude of the scaled demonstrator. However, we can match the scaled outer mold line (OML), angle of attack, and scaled stiffness. In that case, the final in-flight shape of the wing of the scaled demonstrator, as well as the load distribution, are not scaled

versions of the ones on the reference wing at the reference conditions. This is because for a given geometry at a certain angle of attack, the aerodynamic loads are not equivalent unless the nondimensional parameters are the same.

To understand the effect of Mach number, we can use the Prandtl–Glauert (1928) correction to provide an estimate of the aerodynamic forces at high subsonic Mach numbers based on the forces computed in the incompressible regime ($M < 0.3$). The Prandtl–Glauert correction for the lift coefficient of a two-dimensional airfoil is given by

$$C_l = \frac{C_{l_0}}{\sqrt{1-M^2}}, \tag{1}$$

where $C_{l_0}$ is the lift coefficient at incompressible conditions, which in turn is given by

$$C_{l_0} = \frac{l_0}{\frac{1}{2}\rho V^2 c}, \tag{2}$$

where $l_0$ is incompressible lift per unit span.

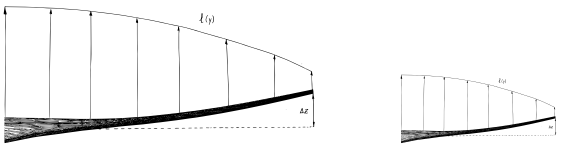

(a) (b)

Fig. 1: Reference wing deflection and load distribution (a) and its scaled counterpart when complete aeroelastic similarity exists (b).

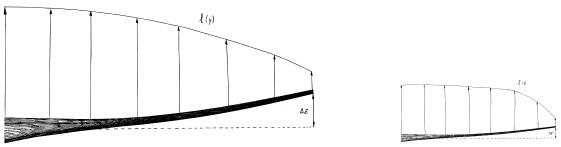

(a) (b)

Fig. 2: Reference wing deflection and load distribution (a) and its scaled counterpart when there is no flow similarity (b). In that case, the wing deflection and loading are no longer similar.

If we tried to reproduce the static aeroelastic behavior of a typical airliner ($M \sim 0.85$) using a model with scaled stiffness, shape, and angle of attack flying at a lower Mach number (e.g., $M \sim 0.3$), we would find that the aerodynamic loads, and hence the displacements, would be noticeably lower, according to the Prandtl–Glauert (1). This is illustrated by Figure 2 and shown with a particular example of application on Section 5.

If we now consider the case where we attempt to optimize the wing geometry and structural properties at the same time to match the static aeroelastic deflections despite significant differences in the flow nondimensional parameters, we cannot use the nondimensional analysis of the aerodynamic equations, as in this case the scaled OML is not preserved. In that case, we need the in-flight deflections of the reference aircraft for a particular angle of attack. To evaluate the fitness of a particular design, we need to perform a complete static aeroelastic analysis for the given design variables and the Mach number of the scaled demonstrator. Then we can compare the in-flight shape to the scaled version of the reference one and evaluate the lift and stress constraints.

### 2.2 Aeroelastic Multidisciplinary Analysis

In this paper, we use Panair (Magnus and Epton, 1980), a panel aerodynamics code implementing the Prandtl–Glauert compressibility corrections coupled to Nastran95 (MacCormick, 1972), a finite element solver. An independent aerodynamic analysis is performed for each deformed configuration of the wing. The XDSM (Lambe and Martins, 2012) diagram corresponding to this MDA is shown in Figure 3. Within each MDA cycle, the aerodynamic loads are computed and transferred to the FEM model. Then, the structural displacements are solved for and interpolated back on the aerodynamic grid. We have two flight conditions: cruise (to ensure steady flight), and limit load (to ensure structural integrity). Therefore, a separate MDA is solved for each one.

### 2.3 Optimization Formulation

Once we have established the MDA for this problem, we present the formulation of the optimization problem. To solve the optimization problem, we adopt the multidisciplinary feasible (MDF) approach, which is described by Martins and Lambe (2013). Using the MDF approach, the complete MDA is solved completely for each iteration of the design variables. This approach is both easy to implement and computationally efficient. Figure 4 shows the XDSM for the aeroelastic optimization. Because each optimization loop includes an MDA for each angle of attack $\alpha_i$, they are represented in a stacked manner as they can be performed independently. One of the goals of this study is to ensure that the scaled aerodynamic loads and wing deflections of the scaled model are equivalent to the ones of the reference aircraft for the same angles of attack. In that

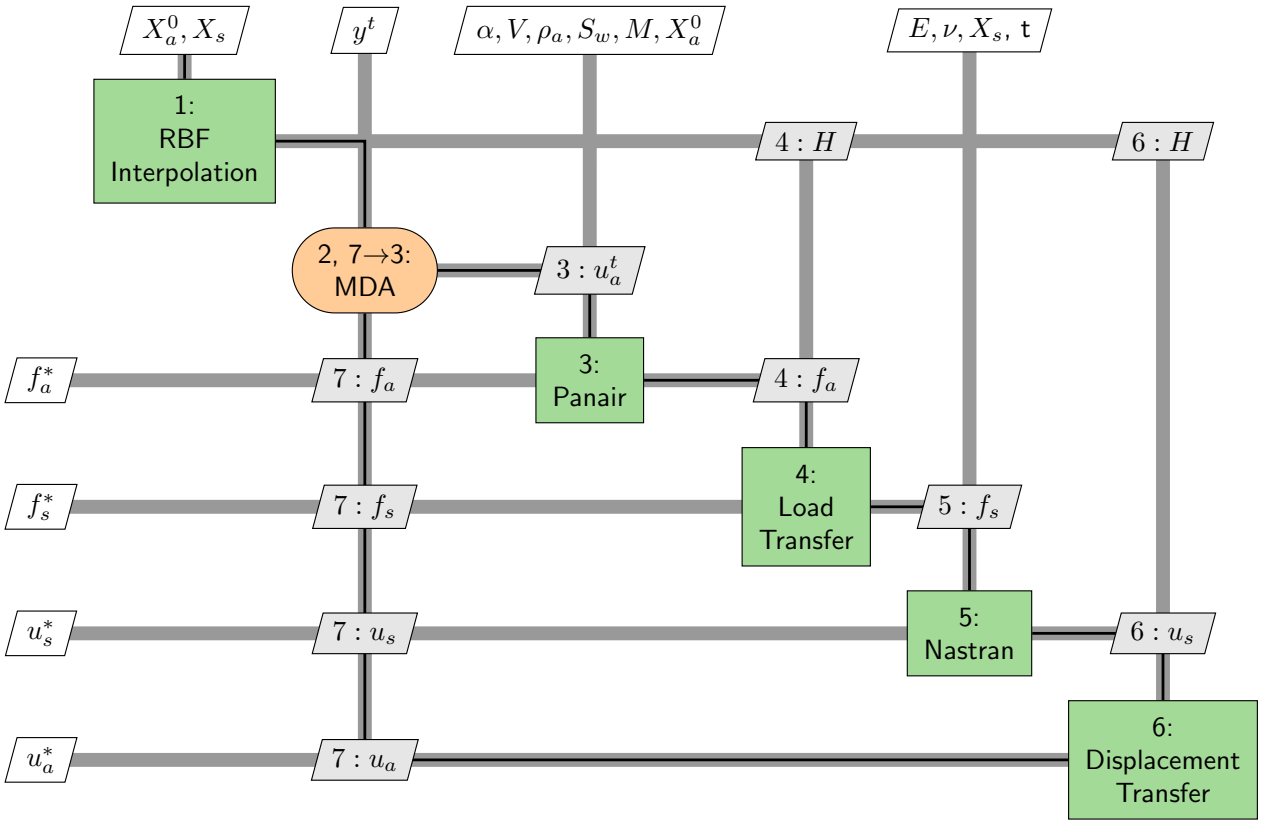


Fig. 3: XDSM diagram for the static aeroelastic MDA.

manner, the response of the scaled wing loads and displacements with respect to the angle of attack is similar. The values of $\alpha_i$ correspond to fixed values of the angle of attack for which the lift force on the reference aircraft is known.

The goal of this optimization problem is to find the wing design parameters that minimize the error in the in-flight shape with respect to the scaled wingtip deflection of the reference aircraft while keeping the similarity at certain angles of attack. For that purpose, we require the scaled lift to be matched for two angles of attack. By doing so, we ensure that the derivative of the aerodynamic load with respect to the angle of attack $C_{L\alpha}$ is preserved. If similarity of airflow, aerodynamic shape, and wing elasticity existed between the reference aircraft and the scaled model, the identity of $C_{L\alpha}$ would be automatically satisfied. Since in our case similarity in airflow and external shape is no longer preserved, we ensure the equality of $C_{L\alpha}$ using optimization constraints.

To ensure the structural integrity for the most critical flight condition, we require the von Mises stress in any point of the wingbox structure to be lower than the allowable stress of the structural material for the $+2.5g$ maneuver condition.

The optimization problem formulation that we propose is

$$
\begin{aligned}
\text{minimize} \quad & f = \|\mathbf{u}_{\text{tip}}^{\mathbf{m}} - \lambda_l \mathbf{u}_{\text{tip}}^{\mathbf{r}}\|_2^2 \\
\text{w.r.t.} \quad & x \in \mathbb{R}^n \\
\text{subject to:} \quad & \frac{C_L^{m,c} - C_L^{r,c}}{C_L^{r,c}} = 0, \\
& \frac{C_L^{m,2.5g} - C_L^{r,2.5g}}{C_L^{r,2.5g}} = 0, \\
& \frac{\max(\sigma_{VM}) - \sigma_y}{\sigma_y} \leq 0, \\
& x_{\frac{c}{2}}^{m,r} - \lambda_l x_{\frac{c}{2}}^{r,r} = 0, \\
& x_{\frac{c}{2}}^{m,b} - \lambda_l x_{\frac{c}{2}}^{r,b} = 0, \\
& x_{\frac{c}{2}}^{m,t} - \lambda_l x_{\frac{c}{2}}^{r,t} = 0,
\end{aligned}
\tag{3}
$$

where $\mathbf{u}_{\text{tip}}^{\mathbf{m}}$ is the wingtip displacement vector of the scaled model wing during cruise flight, $\mathbf{u}_{\text{tip}}^{\mathbf{r}}$ is the corresponding quantity for the reference aircraft, and $\lambda_l$ is the overall geometrical scale factor (i.e., wing span ratio). The objective is to minimize the squared norm

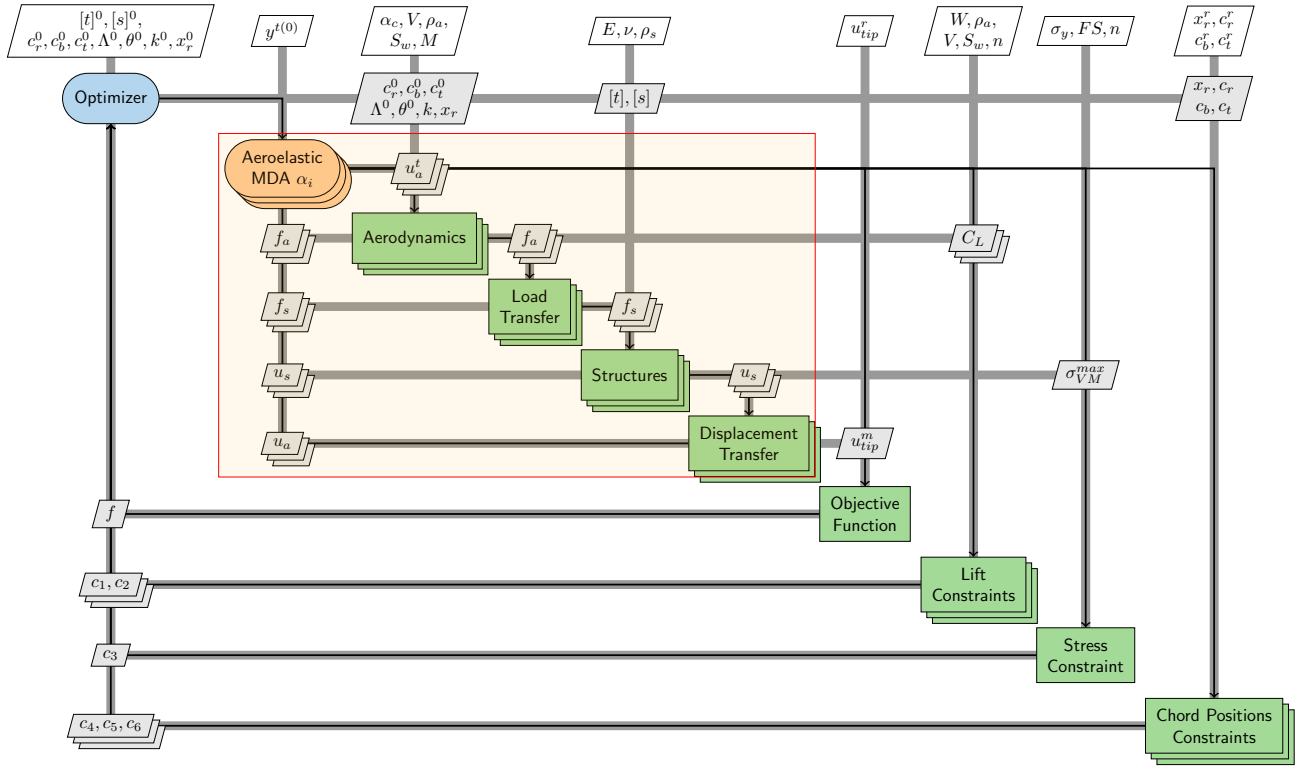


Fig. 4: XDSM diagram for the static aeroelastic MDAO. The orange box represents the MDA cycle. Several MDA cycles are stacked (one for each angle of attack) since they are performed independently one from another.

of the difference between the scaled reference displacement vector of the wingtip and the one of the scaled model. Thus, we find a wing with a similar overall flexibility while ensuring that the total scale wing load is equivalent.

The nondimensional lift is matched through the lift coefficients, which are already nondimensional. The cruise lift coefficient of the reference aircraft is

$$C_L^{r,c} = \frac{W_r g}{\frac{1}{2}\rho_r V_r^2 S r}, \tag{4}$$

where $W_r$ is the weight (in units of mass) of the reference aircraft. For the case of the scaled model, the lift coefficient is

$$C_L^{m,c} = \frac{L_{\alpha=\alpha_c}}{\frac{1}{2}\rho_m V_m^2 \lambda_l^2 S r}. \tag{5}$$

In Eq. (5), the reference surface is $\lambda_l^2 S_r$ and not the actual wing surface of the model wing. This is because we want to match the scaled lift of the reference aircraft (which is determined by $\lambda_l$) for the reference cruise angle of attack. For the lift constraint at $2.5g$, the definition of the lift coefficient is the same except that the apparent weight is now $2.5W$, and the lift force is computed at the angle of attack that produces that lift on the reference aircraft ($\alpha = \alpha_{2.5g}$).

The inequality constraint on Eq. (3) ensures that the von Mises stress for any element on the structure is lower than the allowable stress, at the $2.5g$ maneuver condition, as defined by the Civil Aviation Regulations FAR-25 (2020). Since the optimizer that we use to solve this problem does not require the derivatives of the objective function and constraints, we use the max() function applied to the von Mises stress of all elements—whose derivatives might are continuous. The last three equality constraints in Eq. (3) ensure that the longitudinal positions of the mid-chord points of the three characteristic wing sections of the scaled model remain the same as the scaled longitudinal positions of the reference aircraft.

In the next section, we apply this optimization formulation a scaled version of the undeflected Common Research Model (uCRM) wing (Brooks et al., 2018).

## 3 Methods and Tools

### 3.1 Method for Displacement and Load Transfer

In this section, we present the method for force and displacement transfer between the aerodynamics and structures disciplines, which is needed for the MDA described in the previous section.

The aerostructural MDA involves four state vectors: the displacements of the structure nodes $\mathbf{u_s}$, the displacements of the aerodynamic mesh $\mathbf{u_a}$, the forces acting on the aerodynamic grid points $\mathbf{f_a}$, and the aerodynamic forces acting on the nodes of the structural model $\mathbf{f_s}$.

Given that the grid points of the structural and aerodynamic models do not coincide, it is necessary to transfer the displacements on the structural nodes $u_s$ to the aerodynamic mesh to determine its displacements $u_a$. We use the displacement and load transfer method described by Rendall and Allen (2008). This method is based on creating a displacement field that satisfies the interpolation condition on the structural nodes, on which the displacements are known from the FEM analysis. Through the use of radial basis functions (RBF), defined by Broomhead and Lowe (1988), each one of the three components of the displacement field (we write the equation for the $x$ component, but the same holds for $y$ and $z$) is written as

$$u_x = \sum_{i=1}^{N_s} \beta_i^x \phi(\|\mathbf{x} - \mathbf{x_i}\|) + \gamma_0^x + \gamma_x^x x + \gamma_y^x y + \gamma_z^x z, \quad (6)$$

where $\mathbf{x}$ is the vector of space coordinates, $\mathbf{x_i}$ represents the nodes at the centers of the radial basis functions, and $\phi(r)$ is the RBF. We chose to use the thin plate spline (TPS) RBF, which can be written as $\phi(r) = r^2 \ln r$. This choice was based on the recommendations given by Lombardi et al. (2013). After comparing many available functions, they concluded that TPS functions yielded the best, most accurate, and most robust results for interpolation because they do not require any parameter tuning. The terms $\beta_i^x$ are the RBF coefficients and $\gamma$ are the coefficients of the linear polynomial part. The interpolated displacement field evaluated on the aerodynamic grid points is obtained through a matrix-vector product from the vector of known structural displacements $\mathbf{u_s}$ and a matrix $[\mathbf{H}]$. This matrix $[\mathbf{H}]$ is obtained by imposing the interpolation condition and by evaluating each RBF on the aerodynamic points. The displacement transfer is then expressed as

$$\mathbf{u_a} = [\mathbf{H}]\mathbf{u_s}, \quad (7)$$

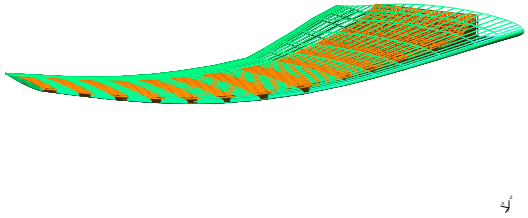

Fig. 5: Transfer of the displacements from the structural grid (orange) to the aerodynamic surface mesh (green).

where $[\mathbf{H}]$ depends only on the positions of the structural nodes and the grid points of the aerodynamic mesh, as well as on the RBF type (such as Gaussian or TPS). Figure 5 illustrates how the displacement field, known at the structure grid (in orange), is transferred to the aerodynamic grid (in green).

Once the displacement transfer matrix is established, Rendall and Allen (2008) determined the matrix for the transfer of the aerodynamic forces from the aerodynamic grid $\mathbf{f_a}$ to the structural nodes $\mathbf{f_s}$. This was done by using the principle of virtual work for the conservation of the energy. The virtual work is

$$\delta W = \delta \mathbf{u_s}^T \mathbf{f_s} = \delta \mathbf{u_a}^T \mathbf{f_a}, \quad (8)$$

where $\delta \mathbf{u_s}$ represent the virtual displacements of the structural nodes used for the displacement interpolation and $\delta \mathbf{u_a}$ are the virtual displacements of the aerodynamic grid points. By using the displacement matrix $[\mathbf{H}]$, the virtual displacements of the aerodynamic grid are

$$\delta \mathbf{u_a} = [\mathbf{H}] \delta \mathbf{u_s}. \quad (9)$$

After substituting Eq. (9) into Eq. (8), the aerodynamic forces on the structural nodes are

$$\mathbf{f_s} = [\mathbf{H}]^T \mathbf{f_a}. \quad (10)$$

The construction of the interpolation matrix for each geometry of the aerodynamic and structural meshes allows us to exchange displacements and forces through a matrix-vector product.

### 3.2 Geometry and Mesh Generation

For the generation of the OML from the planform design variables, we use the baseline uCRM wing geometry for the twist distribution and the vertical coordinates of the wing sections. The airfoil shapes are those of the original CRM wing, including the relative

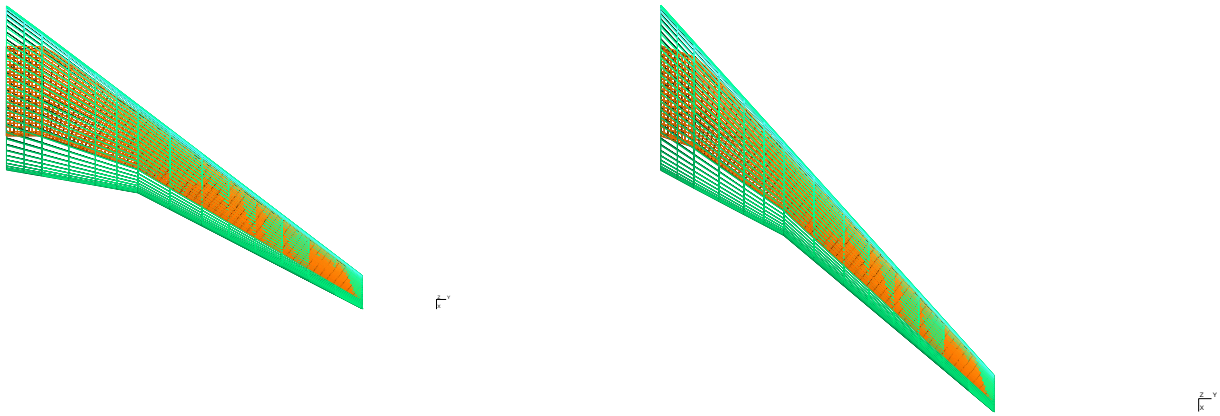

Fig. 6: The structural mesh (orange) is initially known only in its baseline configuration (left). Through the new shape of the OML (in green), it is automatically adapted to new shape using the RBF methodology (on the right). For illustration purposes, the sweep is increased while keeping chords and span constant.

thickness, relative camber, and spanwise position of the wing sections. This baseline geometry defines the airfoil shape and twist at eight sections from the root to the wingtip. The planform design variables determine the leading edge position and chord length. The spanwise and vertical position of the sections, as well as their relative thickness and camber, are kept constant. The values for these correspond to the scaled reference wing. From this definition of the wing through its section properties, we define the jig OML corresponding to each set of design variables.

The OML and a structured surface mesh for the aerodynamics panel code are generated using the GMSH software package, developed by Geuzaine and Remacle (2009). For each vector of design variables, the topology of the structured surface mesh remains the same.

The geometric variables described above first determine the shape of the jig OML, which then determines the new shape of the jig wingbox. To find the structural wingbox geometry for a given OML, we use a morphing technique based on the RBF method that we used for the interpolation of displacements, defined by Rendall and Allen (2008) (see Section 3.1). This is done by treating the changes in the OML as displacements, which are interpolated to find the corresponding changes to the wingbox geometry and mesh, as shown in Figure 6.

## 4 Application to the Scaled uCRM Wing

In the previous section, we defined the optimization problem used to match the static aeroelastic behavior of scaled demonstrators when flow similarity cannot be achieved. In this section, we apply the aforementioned methodology to a scaled version of the uCRM wing. The uCRM wing, established by Brooks et al. (2018), is based on the original CRM wing, defined by Vassberg et al. (2008), and represents the jig shape of a wing such that when in flight its shape matches the CRM one at its nominal flight condition.

### 4.1 Definition of the Scaling Factors

In this example problem, we consider, as the reference wing, the uCRM wing flying at $35,000$ ft and $M = 0.85$ with an aircraft weight of $500,000$ lbm ($\sim 226796$ kg) [1] For the scaled model, whose design we establish through optimization, we consider a reduced model scaled by an overall factor $\lambda_l = 1/5$. For the flight conditions of the model, we consider an altitude of $2,000$ m ($\sim 6,562$ ft). From the Froude number matching, as described by Pires (2014), the scaled airspeed is $V_m = \sqrt{\lambda_l} V_r = 112.77$ m/s. At the scaled model altitude, and using the international standard atmosphere model, this yields a Mach number of $M = 0.34$.

As described by Pires (2014), the scaling factor and the air density ratio $\lambda_\rho = \rho_m/\rho_r$ determine the total mass of the scaled model,

$$W_m = \lambda_\rho \lambda_l^3 W_r, \tag{11}$$

which dictates the amount of lift that needs to be produced for the several flight conditions.

[1] https://commonresearchmodel.larc.nasa.gov/files/2014/02/CRM_wingboxFEM_description_1.pdf

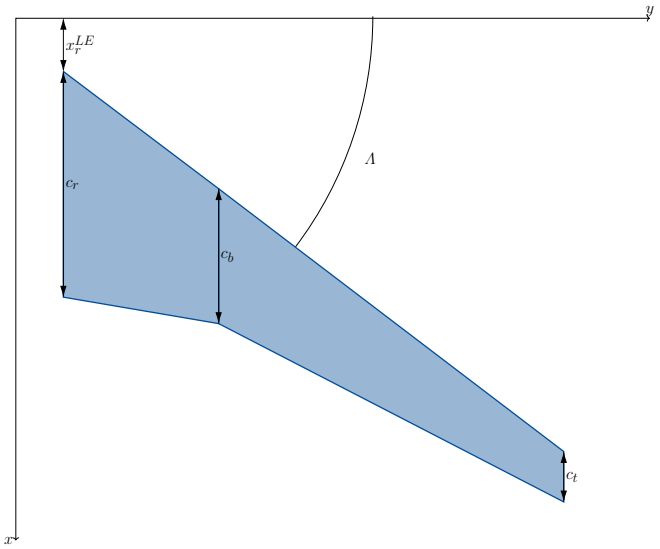


Fig. 7: Planform variables for the static optimization problem: longitudinal position relative to the fuselage $x_r^{LE}$, sweep angle $\Lambda$, root chord $c_r$, break chord $c_b$, and tip chord $c_t$.

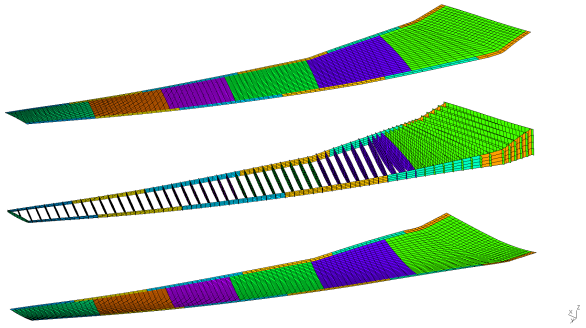

Fig. 8: Thickness regions for the FEM model, which consists of 12,475 shell elements and 10,804 nodes.

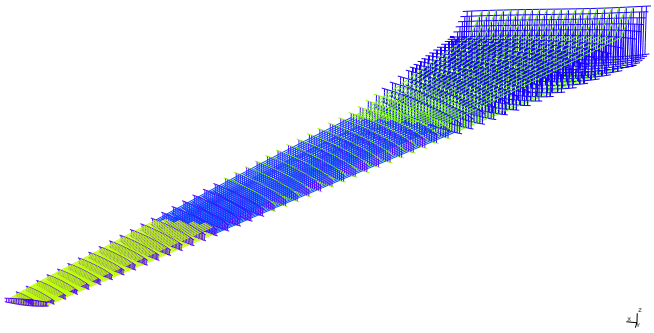

Fig. 9: Stringer property regions for static optimization. The FEM model contains 14,134 bar elements.

### 4.2 Design Variables

The geometric design variables of this problem are the chord lengths at three span sections (root, break, and tip—$c_r$, $c_b$, and $c_t$ respectively), the sweep angle $\Lambda$, the wing mounting angle (the angle between the root section of the wing and the longitudinal axis of the fuselage), as well as the longitudinal position of the wing leading edge at the root. The thickness-to-chord ratio of the sections is obtained by multiplying the baseline distribution of relative thicknesses along the wing span by a scaling factor $k$. We also set $k$ as a design variable to control the flexibility of the wing structure through the height of the wingbox. For the aerodynamic analysis, we define the angle of attack as the angle of the longitudinal axis of the fuselage with respect to the incoming airflow. The geometric planform variables are illustrated in Figure 7.

The structural design variables are the plate thicknesses of the shell elements of the wingbox, as well as the stringer section modeled by beam elements. For the definition of the shell thicknesses, the wingbox is divided into a total of 12 different thickness regions: 6 of them define the thickness of the upper, skins lower skins, and ribs, at 6 wing segments along the span. The other 6 regions define the thickness of the elements on the front and rear spars: the two flanges and the web. These regions of different thickness are shown in Figure 8.

For the stringer sections, there are a total of six variables that define the cross-section values of all the stringers in the model, which belong to six different groups. These regions of different stringer sections are displayed on Figure 9. With these structural design variables, we can tailor the wingbox stiffness.

In contrast to the usual structural optimization problems that aim to improve the performance of an existing design, here we aim to find the whole design of the scaled wing.

The displacement interpolation matrix [**H**] (defined in Section 3.1) has to be recalculated for each optimization iteration before performing the MDA. This is because [**H**] depends on the coordinates of both aerodynamic and structural meshes, as shown in Figure 19.

### 4.3 Definition of the Reference Quantities

According to the optimization problem formulation (3), we need the wingtip displacements of the in-flight reference wing. To obtain them, we perform an MDA loop with the baseline full-scale wing geometry and structure at the nominal flight conditions. To find the correct angle of attack, we perform several iterations until

the generated lift matches the reference aircraft weight, $W_r g$. To determine the angle of attack at the limit load condition, we perform the same operation, but with a target lift of 2.5 times the weight of the reference aircraft. This yields a cruise angle of attack of $\alpha_c = 1.34°$ and $\alpha_{2.5} = 9.66°$ for the limit load condition.

The reference document for the CRM finite element model specifies the following elastic properties: Elastic modulus $E = 68900$ MPa, Poisson's ratio $\nu = 0.31$, and density $\rho_s = 2795.67$ kg/m$^3$. Since the allowable stress is required to evaluate the stress constraint and that this value is not available in the CRM report, we use the maximum von Mises stress computed for the baseline wing at $2.5g$. This yields a yield stress of about 600 MPa, which is representative of a 7068 aluminum alloy.

If we used an aluminum alloy with a lower allowable stress than the maximum observed on the reference wing at limit load condition, the target displacements could probably not be matched, since the flexibility of the scaled wing would be limited by the stress constraint. In that case, the optimizer would need to increase the structural thicknesses to satisfy the stress constraint, thus reducing the required flexibility to match the in-flight shape.

### 4.4 Optimization Problem Setup

The objective function and all the constraints are evaluated for each optimization iteration at the end of the MDA cycle. Figure 4 shows the XDSM diagram of the optimization problem described in this section. A more detailed version of this diagram is shown in the Appendix 6. The optimization problem is summarized in Table 1, which lists the 25 design variables with the corresponding bounds and 6 constraints. The values of $[t_0]$ and $[s_0]$ are estimates for the structural thicknesses and stringer cross-section variables, and are obtained in the same manner as for the modal scaling problem, in Section 4.5, as described by Eqs. (19) and (22). For the values $c_r^0$, $c_b^0$, and $c_t^0$, they are obtained by scaling the baseline section chords by the overall scaling factor $\lambda_l$.

The optimization algorithm we use is COBYLA (Powell, 1994), a gradient-free optimizer, available within the SciPy library (Jones et al., 2001). We use this approach because neither Panair or Nastran95 provide the derivatives of their outputs.

### 4.5 Establishing the starting point

For the scaling of the natural frequencies and the overall mass, Pires (2014) detailed how to obtain the ratios $\lambda$ between the scaled quantities and the reference ones, which are

$$\lambda_\omega = \frac{1}{\sqrt{\lambda_l}}, \tag{12}$$

and

$$\lambda_m = \lambda_\rho \lambda_l^3. \tag{13}$$

Given that the COBYLA optimization path depends on the starting point, we developed a method for finding a set of design variables that is close enough to the optimum. This method is based on the Euler–Bernoulli beam theory and the bending properties of thin-walled structures to find an approximation for scale-down factors of the thicknesses of the structural panels and stringer sections. We consider a cantilever beam of length $L$ (corresponding to the full scale), bending inertia $I$, total mass $m$, and Young's modulus $E$. We start by computing the bending inertia $I'$, whose length and height are scaled according to the ratio $\lambda_l = L'/L$. The overall length ratio affects the length, height, and width of the beam uniquely. Since we assume that the same material is used for both beams, $E' = E$. The two beams are shown in Figure 10.

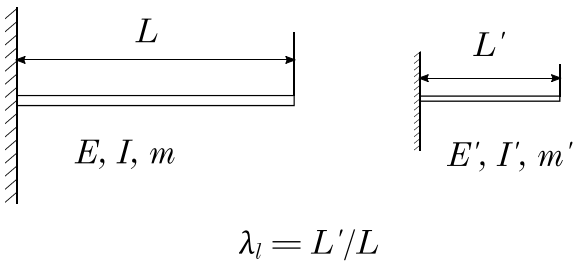


Fig. 10: Full scale and scaled cantilever beams.

By considering the equation for the natural frequencies of the bending modes of a cantilever beam

$$\omega_i = \frac{K_i}{L^2}\sqrt{\frac{EIL}{m}}, \tag{14}$$

where $K_i$ denotes the constant value that depends on the vibration mode, we obtain the frequency ratio as

$$\lambda_\omega = \frac{\omega_i'}{\omega_i} = \frac{\frac{K_i}{L'^2}\sqrt{\frac{E'I'L'}{m'}}}{\frac{K_i}{L^2}\sqrt{\frac{EIL}{m}}}. \tag{15}$$

| **Objective Function** | | **Dimension** |
|---|---|---|
| In-flight shape difference minimization | $f = \|\mathbf{u}^{\mathbf{m}}_{\text{tip}} - \lambda_l \mathbf{u}^{\mathbf{r}}_{\text{tip}}\|_2^2$ | 1 |
| **Design Variables** | | |
| Thicknesses vector | $\mathbf{t}$ | 12 |
| Stringer section vector | $\mathbf{s}$ | 6 |
| Root chord | $c_r$ | 1 |
| Break chord | $c_b$ | 1 |
| Tip chord | $c_t$ | 1 |
| Sweep | $\Lambda$ | 1 |
| Wing mounting angle | $\theta_r$ | 1 |
| Root leading edge | $x_r$ | 1 |
| Relative thickness scaling factor | $k$ | 1 |
| | **Total design variables:** | **25** |
| **Constraints** | | |
| Lift constraints | $\frac{C_L^{m,i} - C_L^{r,i}}{C_L^{r,i}} = 0$ | 2 |
| Stress constraint | $\frac{\max(\sigma_{VM}^{2.5g}) - \sigma_y}{\sigma_y} < 0$ | 1 |
| Longitudinal positions of the chord centers | $x_{\frac{c}{2}}^{m,i} - \lambda_l x_{\frac{c}{2}}^{r,i} = 0$ | 3 |
| | **Total constraints:** | **6** |

Table 1: Optimization problem statement of the uCRM wing. The baseline thickness [$\mathbf{t^0}$] and cross-section [$\mathbf{s^0}$] vectors are the ones defined in Section 4.5, as the design variables and the scale are the same. For the baseline chords, the values are: $c_r^0 = 2.72$ m, $c_b^0 = 1.45$ m, and $c_t^0 = 0.55$ m.

Substituting Eqs. (12) and (13) into Eq. (15), we get

$$\lambda_I = \frac{I'}{I} = \lambda_\rho \lambda_l^5. \tag{16}$$

After establishing the bending inertia ratio $\lambda_I$, we determine the thickness and stringer section ratios, $\lambda_t$ and $\lambda_s$, respectively. By making assuming that the thickness of the beam flanges ($t$) are much smaller than their distance from the neutral axis ($h$), we estimate the contribution of a flange of width $w$ (shown in Figure 11) to the bending inertia of the beam $I$ as

$$\Delta I_t = wth^2. \tag{17}$$

We determine the bending inertia ratio by applying Eq. (17) to the geometrically scaled beam

$$\lambda_I = \frac{w't'h'^2}{wth^2} = \lambda_l^3 \lambda_t. \tag{18}$$

Then, we establish the thickness ratio for the initial design as

$$\lambda_t = \lambda_\rho \lambda_l^2. \tag{19}$$

In a similar manner as presented above for the thickness ratio, we compute the contribution of a stringer placed at a distance $h$ from the neutral axis with a cross-section $s$ (see Figure 12) as

$$\Delta I_s = sh^2. \tag{20}$$

Then, the bending inertia ratio of the contribution of the stringer is

$$\lambda_I = \frac{s'h'^2}{sh^2} = \lambda_l^2 \lambda_s. \tag{21}$$

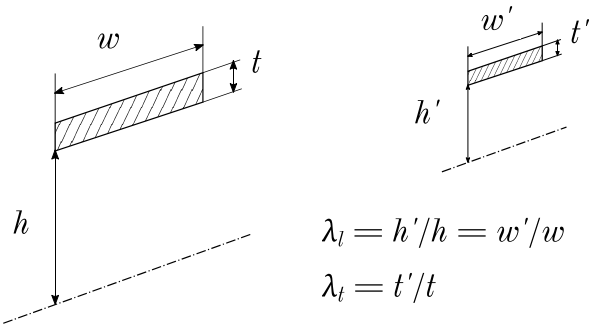


Fig. 11: Plate thicknesses on different scaled beams.

As in the case for the plate thickness ratio, we find the ratio of stringer cross-sections by substituting Eq. (16) into Eq. (21), thus giving

$$\lambda_s = \lambda_\rho \lambda_l^3. \tag{22}$$

Using this method, we obtain a first guess of thicknesses and cross-sections of the different components of the structure that we aim to scale, to use it as the initial set of design variables for the optimizer. We obtain these design variables by simply multiplying the thicknesses and cross-sections of the full-scale model by $\lambda_t$ and $\lambda_s$, respectively.

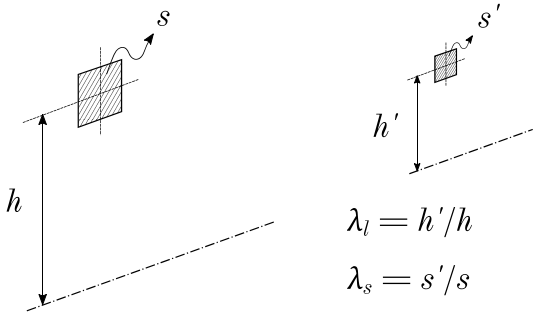


Fig. 12: Stringer sections on different scaled beams.

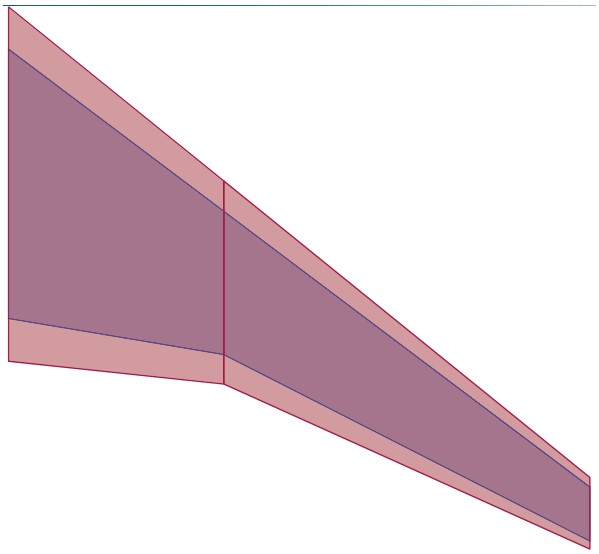

Fig. 13: To compensate for the lift loss due to lower Mach, the optimized planform (red) has an increased wing area compared to the scaled reference planform (blue).

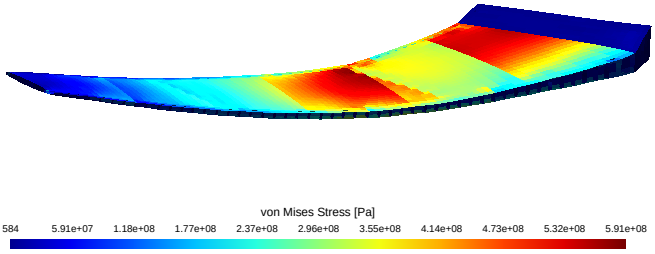


Fig. 14: Stress distribution (von Mises) for the limit load condition of the best design found. Values in Pa.

## 5 Results and Discussion

As previously mentioned we used the gradient-free optimizer COBYLA (Powell, 1994) to solve the optimization problem (3). The stopping criterion is based on the absolute tolerance on the size of COBYLA's trust region, which we set to $10^{-3}$.

The optimization history (Figure 15) shows that the optimum satisfies the stress constraint. The objective function (the wingtip displacement error) converged to 1.5%. Both lift constraints—the cruise condition one and the limit load condition—are satisfied within an error lower than 1%. The lift constraint at the cruise condition has an error lower than 0.1%. The three equality constraints—shown on Figure 16—show that the longitudinal positions of all the wing sections are well preserved for the best design found. This can also be visualized on the optimized planform (Figure 13). The optimization history shows that promising values of the objective function that satisfy the stress constraint were already found before iteration 100. However, the lift constraints are much below zero for such cases. These probably correspond to wing designs with a very low flexibility that reached the desired level of wing displacement, but under a wing load lower than the target value. The in-flight shape corresponding to the optimized design is shown on Figure 18.

To see the importance of performing an aerodynamic and structural re-design when the Mach number cannot be matched, we compute the errors in terms of loads and displacement if the aerodynamic geometry and scaled flexibility of the reference aircraft were left constant. To do so, we present the results that we would get if we used the exact scaled aerodynamic geometry of the reference aircraft along with a structure having the exact scaled shape and the scaled stiffness and using the flight Mach value corresponding to the scaled demonstrator conditions. In that case, whose in-flight shape is shown on Figure 17, the error in terms of the air loads is 16%, while the error in wingtip displacement is 17.5%. These results show that the proposed method can be used effectively to ensure loads and displacements similarity if the airflow conditions of the scaled model are substantially different to the ones of the reference aircraft.

After having presented the results of the last example of application, in the following section we present the conclusions and perspectives of this paper.

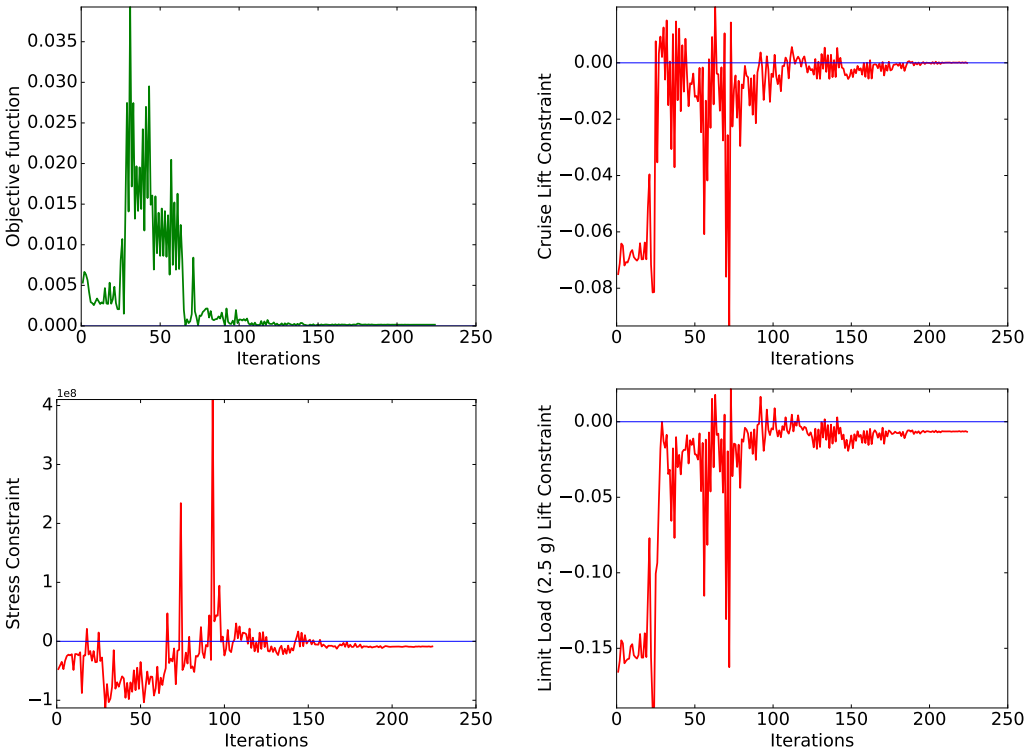


Fig. 15: Evolution of the objective function, the maximum stress constraint, and the two lift constraints with the number of iterations.

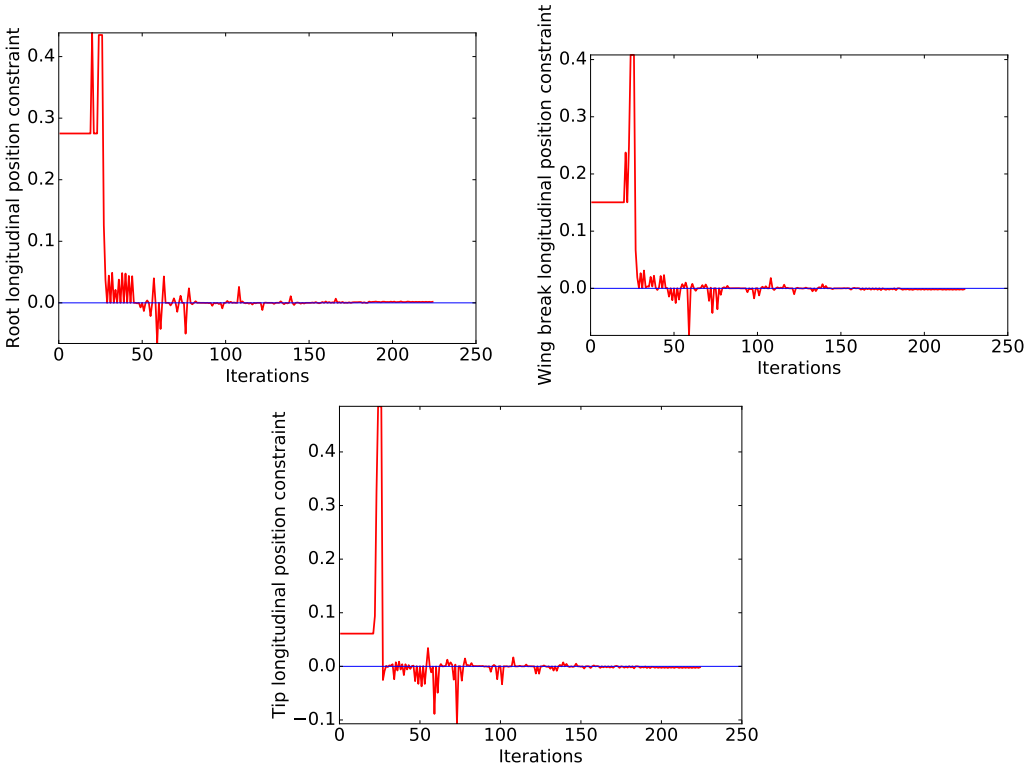


Fig. 16: Evolution of the equality constraints for the longitudinal positions of the root, break, and tip sections.

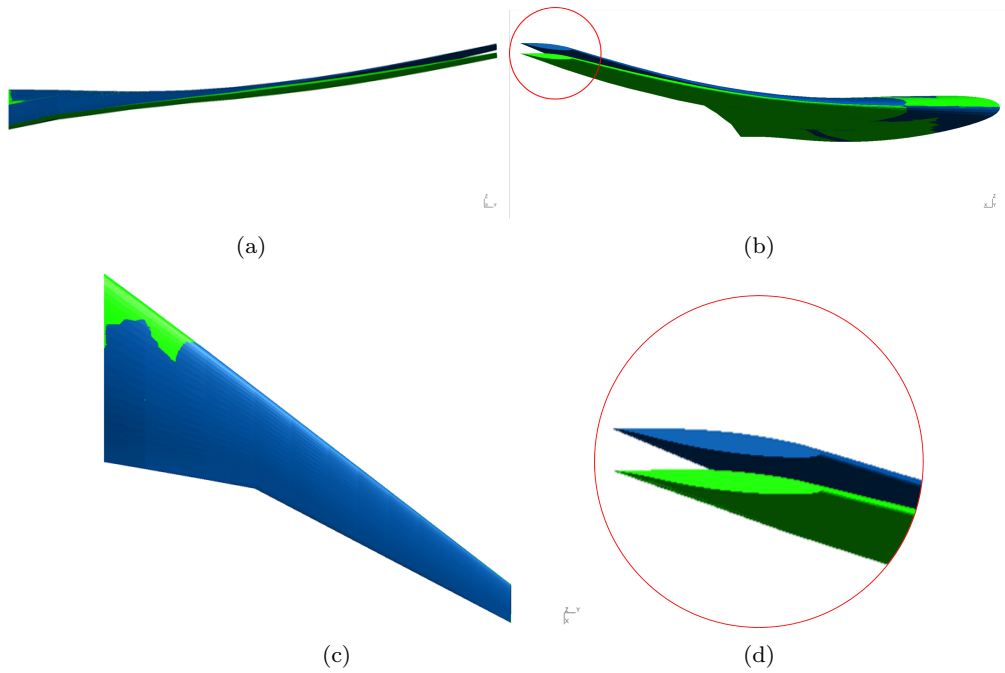

(a) (b)

(c) (d)

Fig. 17: Not using any re-design to account for difference in Mach number leads to a discrepancy between the wingtip displacement of the reference wing under reference conditions (blue) and the same scaled wing in test conditions (green). Front view (a), side view (b), top view (c), and detail of the wingtip (d).

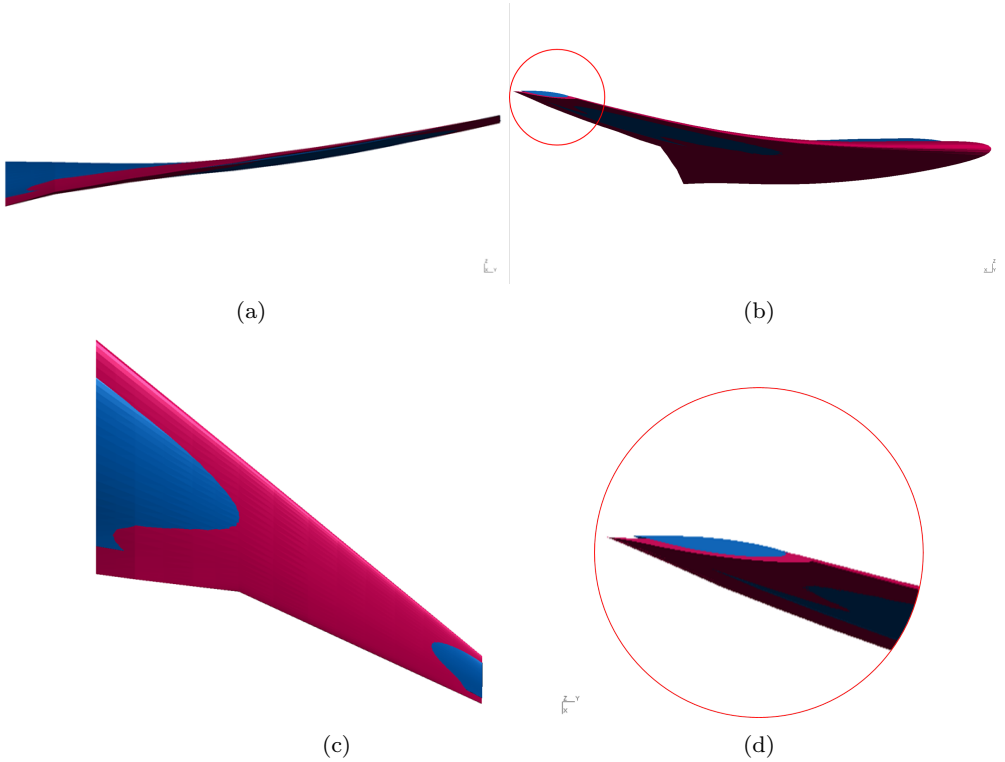

(a) (b)

(c) (d)

Fig. 18: The wingtip displacement of the optimized design (red) matches the one of the target shape (blue). Front view (a), side view (b), top view (c), and detail of the wingtip (d).

## 6 Conclusion

In this paper, we maximize the similarity of the static response of the wing as a whole (i.e., in terms of the total air load and the overall wing deflection). This enables to assess the aeroelastic qualities of a certain wing concept, but not to extrapolate local data of the airflow or the structural response of the full-scale aircraft.

The dominant effect of operating the scaled model at a lower Mach number than its full scale counterpart is the reduction in the lift forces for the same angle of attack. With the baseline geometry and scaled stiffness, the relative error in the total air load in cruise flight is 16%, while the relative error in the wingtip displacement is 17.5%. These substantial errors justify the changes in the wing geometry and the structural properties when the airflow conditions change substantially. With the optimized wing, we observe an increase in the area to produce equivalent lift with the imposed angles of attack of the reference conditions. The results show a good in-flight shape matching, with an error of less than 1% in the lift constraints. Since the shape of the wing is modified, which has an impact on the structural stiffness, the properties of the structural components are modified accordingly to give the wing the appropriate stiffness in spite of the changes in geometry.

The results in this paper are obtained using the panel method with compressibility corrections. However, more physically accurate results could be obtained by using the same optimization formulation and simply replacing the current aerodynamic model by a more realistic CFD analysis.

**Acknowledgements** This work is part of the activities of ONERA–ISAE–ENAC joint research group. This work was funded by the Airbus CEDAR Chair and the EU Project 658570—NextGen Airliners.

## Appendix

### 6.1 Complete XDSM Diagram of the Static Aeroelastic Optimization Problem

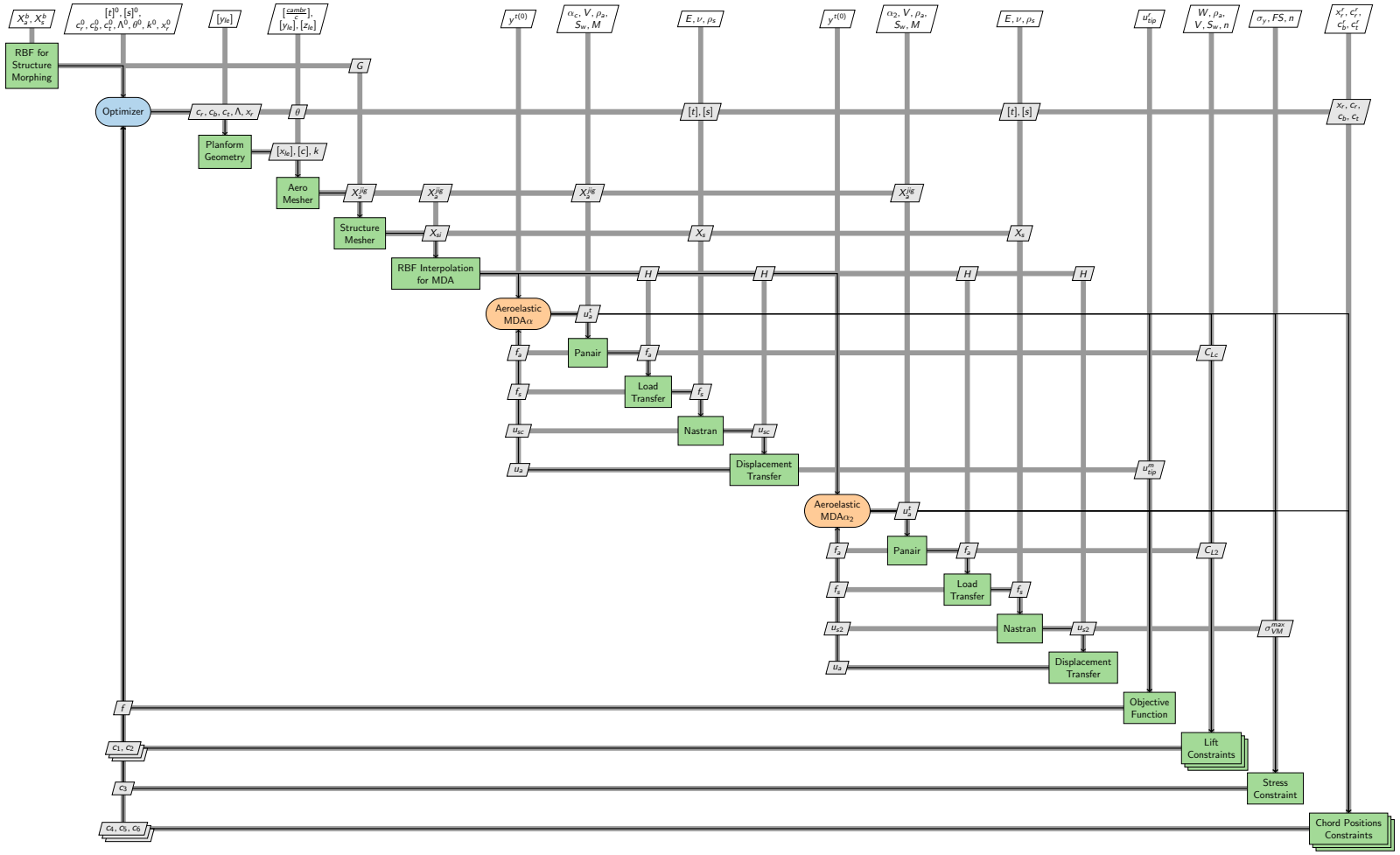


Fig. 19: XDSM diagram for the static aeroelastic MDAO. The first MDA loop determines the cruise angle of attack to evaluate the objective function as well as the cruise lift constraint. The second MDA loop determines the angle of attack of the limit load condition to evaluate the lift constraint at the limit load as well as the stress constraint. Both MDAs are independent from each other and can be executed in parallel.

## Conflict of interest

On behalf of all authors, the corresponding author states that there is no conflict of interest.

## Replication of results

The results presented in this paper can be replicated using the publicly available data of the CRM wing (Vassberg et al., 2008), the uCRM wing (Brooks et al., 2018), as well as the open-source structural solver NASTRAN95 (MacCormick, 1972), and the open-source aerodynamics solver PANAIR (Magnus and Epton, 1980).

## References


Afonso F, Vale J, Oliveira E, Lau F, Suleman A (2017) A review on non-linear aeroelasticity of high aspect-ratio wings. Progress in Aerospace Sciences 89:40–57, doi:10.1016/j.paerosci.2016.12.004, URL http://linkinghub.elsevier.com/retrieve/pii/S037604211630077X

Bisplinghoff RL, Ashley H, Halfman RL (1996) Aeroelasticity. Courier Corporation

Bond VL, Canfield RA, Suleman A, Blair M (2012) Aeroelastic Scaling of a Joined Wing for Nonlinear Geometric Stiffness. AIAA Journal 50(3):513–522, doi:10.2514/1.41139, URL http://arc.aiaa.org/doi/abs/10.2514/1.41139

Brooks TR, Kenway GKW, Martins JRRA (2018) Benchmark Aerostructural Models for the Study of Transonic Aircraft Wings. AIAA Journal 56(7):2840–2855, doi:10.2514/1.J056603, URL https://arc.aiaa.org/doi/10.2514/1.J056603

Broomhead DS, Lowe D (1988) Radial basis functions, multi-variable functional interpolation and adaptive networks. Tech. rep., Royal Signals and Radar Establishment Malvern (United Kingdom)

Cavallaro R, Demasi L (2016) Challenges, Ideas, and Innovations of Joined-Wing Configurations: A Concept from the Past, an Opportunity for the Future. Progress in Aerospace Sciences 87:1–93, doi:10.1016/j.paerosci.2016.07.002, URL http://linkinghub.elsevier.com/retrieve/pii/S0376042116300471

FAR-25 (2020) Federal Aviation Regulations – Part 25. URL https://www.ecfr.gov/cgi-bin/text-idx?SID=05234956f83336784da3123df4386d13&mc=true&node=pt14.1.25&rgn=div5

French M (1990) An application of structural optimization in wind tunnel model design. In: 31st Structures, Structural Dynamics and Materials Conference, American Institute of Aeronautics and Astronautics, Long Beach, California, doi:10.2514/6.1990-956, URL http://arc.aiaa.org/doi/10.2514/6.1990-956

French M, Eastep FE (1996) Aeroelastic model design using parameter identification. Journal of Aircraft 33(1):198–202, doi:10.2514/3.46922, URL http://arc.aiaa.org/doi/10.2514/3.46922

Geuzaine C, Remacle JF (2009) Gmsh: A 3-d finite element mesh generator with built-in pre-and post-processing facilities. International journal for numerical methods in engineering 79(11):1309–1331

Glauert H (1928) The effect of compressibility on the lift of an aerofoil. Proceedings of the Royal Society of London Series A, Containing Papers of a Mathematical and Physical Character 118(779):113–119

Jones E, Oliphant T, Peterson P, et al. (2001) Scipy: Open source scientific tools for python

Jonsson E, Riso C, Lupp CA, Cesnik CES, Martins JRRA, Epureanu BI (2019) Flutter and post-flutter constraints in aircraft design optimization. Progress in Aerospace Sciences 109:100537, doi:10.1016/j.paerosci.2019.04.001

Kenway GKW, Martins JRRA (2014) Multipoint High-Fidelity Aerostructural Optimization of a Transport Aircraft Configuration. Journal of Aircraft 51(1):144–160, URL http://arc.aiaa.org/doi/abs/10.2514/1.C032150

Lambe AB, Martins JRRA (2012) Extensions to the design structure matrix for the description of multidisciplinary design, analysis, and optimization processes. Structural and Multidisciplinary Optimization 46(2):273–284, URL http://link.springer.com/article/10.1007/s00158-012-0763-y

Lombardi M, Parolini N, Quarteroni A (2013) Radial basis functions for inter-grid interpolation and mesh motion in FSI problems. Computer Methods in Applied Mechanics and Engineering 256:117–131, doi:10.1016/j.cma.2012.12.019, URL http://linkinghub.elsevier.com/retrieve/pii/S0045782513000029

MacCormick CW (1972) The NASTRAN User's Manual:(level 15). National Aeronautics and Space Administration

Magnus A, Epton M (1980) A computer program for predicting subsonic or supersonic linear potential flows about arbitrary configurations using a higher order panel method, vol. i. theory document (version 1.0). NASA Contractor Report 3251

Martins JRRA, Lambe AB (2013) Multidisciplinary design optimization: a survey of architectures. AIAA journal 51(9):2049–2075

Mas Colomer J, Bartoli N, Lefebvre T, Dubreuil S, Martins JRRA, Benard E, Morlier J (2017) Similarity Maximization of a Scaled Aeroelastic Flight Demonstrator via Multidisciplinary Optimization. In: 58th AIAA/ASCE/AHS/ASC Structures, Structural Dynamics, and Materials Conference, American Institute of Aeronautics and Astronautics, Grapevine, Texas, doi:10.2514/6.2017-0573, URL http://arc.aiaa.org/doi/10.2514/6.2017-0573

Pereira P, Almeida L, Suleman A, Bond V, Canfield R, Blair M (2007) Aeroelastic scaling and optimization of a joined-wing aircraft concept. In: 48th AIAA/ASME/ASCE/AHS/ASC Structures, Structural Dynamics, and Materials Conference, American Institute of Aeronautics and Astronautics, Honolulu, Hawaii, doi:10.2514/1.2199

Pires T (2014) LINEAR AEROELASTIC SCALING OF A JOINED WING AIRCRAFT URL https://fenix.tecnico.ulisboa.pt/downloadFile/563345090412707/Dissertacao.pdf

Pontillo A, Hayes D, Dussart GX, Lopez Matos GE, Carrizales MA, Yusuf SY, Lone MM (2018) Flexible High Aspect Ratio Wing: Low Cost Experimental Model and Computational Framework. In: 2018 AIAA Atmospheric Flight Mechanics Conference, American Institute of Aeronautics and Astronautics, Kissimmee, Florida, doi:10.2514/6.2018-1014, URL https://arc.aiaa.org/doi/10.2514/6.2018-1014

Powell MJ (1994) A direct search optimization method that models the objective and constraint functions by linear interpolation. In: Advances in optimization and numerical analysis, Springer, pp 51–67

Rendall TCS, Allen CB (2008) Unified fluid–structure interpolation and mesh motion using radial basis functions. International Journal for Numerical Methods in Engineering 74(10):1519–1559, doi:10.1002/nme.2219, URL http://doi.wiley.com/10.1002/nme.2219

Ricciardi A, Canfield R, Patil M, Lindsley N (2012) Nonlinear Aeroelastic Scaling of a Joined Wing Aircraft. In: 53rd AIAA/ASME/ASCE/AHS/ASC Structures, Structural Dynamics and Materials Conference, American Institute of Aeronautics and Astronautics, Honolulu, Hawaii, doi:10.2514/6.2012-1454, URL http://arc.aiaa.org/doi/abs/10.2514/6.2012-1454

Ricciardi AP, Eger CAG, Canfield RA, Patil MJ (2014) Nonlinear Aeroelastic-Scaled-Model Optimization Using Equivalent Static Loads. Journal of Aircraft 51(6):1842–1851, doi:10.2514/1.C032539, URL http://arc.aiaa.org/doi/10.2514/1.C032539

Ricciardi AP, Canfield RA, Patil MJ, Lindsley N (2016) Nonlinear Aeroelastic Scaled-Model Design. Journal of Aircraft 53(1):20–32, doi:10.2514/1.C033171, URL http://arc.aiaa.org/doi/10.2514/1.C033171

Richards J, Suleman A, Canfield R, Blair M (2009) Design of a scaled rpv for investigation of gust response of joined-wing sensorcraft. In: 50th AIAA/ASME/ASCE/AHS/ASC Structures, Structural Dynamics, and Materials Conference, American Institute of Aeronautics and Astronautics, Palm Springs, California, doi:10.2514/6.2009-2218, URL http://arc.aiaa.org/doi/pdf/10.2514/6.2009-2218

Scruton C, Lambourne N (1971) Similarity Requirements for Flutter Model Testing. In: Manual on Aeroelasticity, AGARD, vol IV, E.C. Pike, pp 1–26, Chap 6, URL https://www.sto.nato.int/publications/AGARD/AGARD-R-578/AGARDR57871.pdf

Spada C, Afonso F, Lau F, Suleman A (2017) Nonlinear aeroelastic scaling of high aspect-ratio wings. Aerospace Science and Technology 63:363–371, doi:10.1016/j.ast.2017.01.010, URL http://linkinghub.elsevier.com/retrieve/pii/S1270963817301074

Vassberg JC, DeHaan MA, Rivers SM, Wahls RA (2008) Development of a common research model for applied CFD validation studies. AIAA paper 6919:2008, URL http://arc.aiaa.org/doi/pdf/10.2514/6.2008-6919

Wan Z, Cesnik CES (2014) Geometrically Nonlinear Aeroelastic Scaling for Very Flexible Aircraft. AIAA Journal 52(10):2251–2260, doi:10.2514/1.J052855, URL http://arc.aiaa.org/doi/10.2514/1.J052855